Supplementary Information

A new helical InSeI polymorph: crystal structure and polarized Raman spectroscopy study

Lucía Olano-Vegas,[a,b] Davide Spirito,[c] Evgeny Modin,[a] Pavlo Solokha,[d] Sergio Marras,[e] Marco Gobbi,[f,g] Fèlix Casanova,[a,g] Serena De Negri,[d] Luis E. Hueso,[a,g]* and Beatriz Martín-García,[a,g]*

[a]CIC nanoGUNE BRTA, 20018 Donostia-San Sebastián, Basque Country, Spain.

[b]Departamento de Polímeros y Materiales Avanzados: Física, Química y Tecnología, University of the Basque Country (UPV/EHU), 20018, Donostia-San Sebastian, Spain

[c]BCMaterials - Basque Center for Materials, Applications, and Nanostructures, UPV/EHU Science Park, Leioa 48940, Spain

[d]Dipartimento di Chimica e Chimica Industriale, Università degli Studi di Genova, Genova 16146, Italy.

[e]Istituto Italiano di Tecnologia - Materials Characterization Facility, Genova 16163, Italy.

[f]Materials Physics Center CSIC-UPV/EHU, 20018 Donostia-San Sebastián, Spain

[g]IKERBASQUE, Basque Foundation for Science, 48009 Bilbao, Spain.

X-Ray diffraction characterization
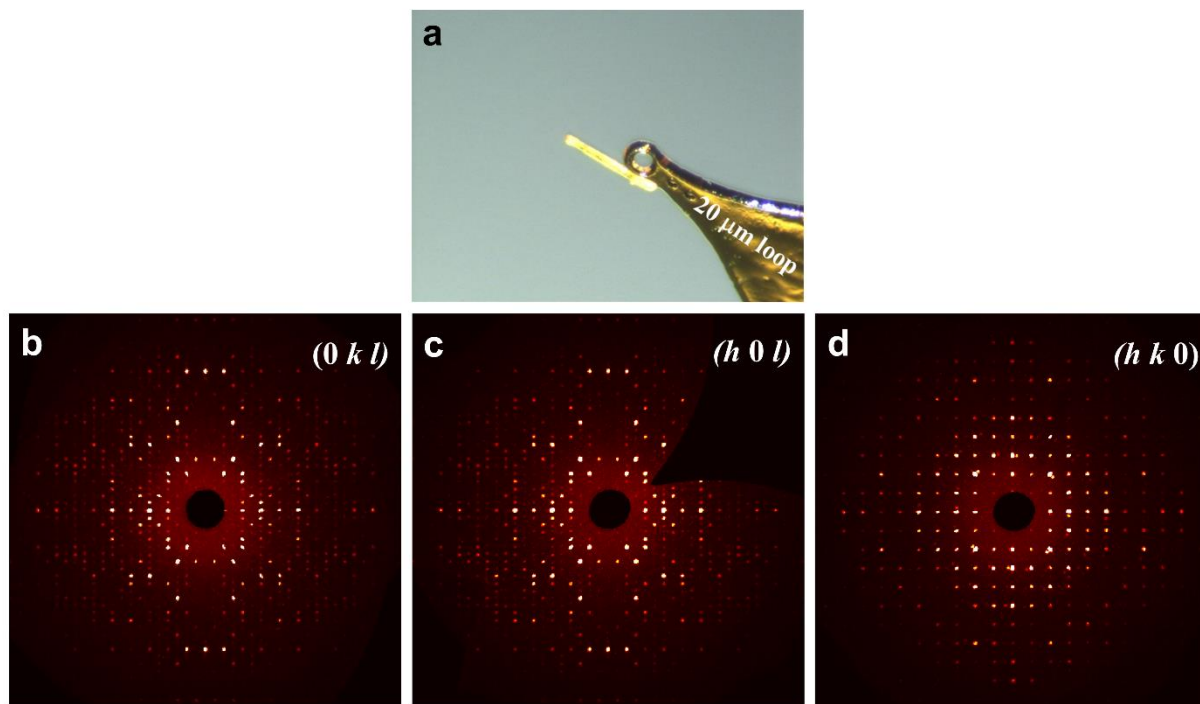
Fig. S1. InSeI crystal selected for structure determination (a); reconstructed precession images for the 0kl (b), h0l (c) and hk0 (d) planes.

|	
Chemical formula	InSeI
Formula weight (g/mol)	320.68
Temperature (K)	293(2)
Wavelength (Å)	0.71076
Crystal system	tetragonal
Space group, Z	P -4, 76
Unit cell dimensions (Å)	a = 18.929(7)
	c = 24.058(10)
Volume (Å^3)	8620.(8)
Density (g/cm^3), calculated	4.695
Absorption coefficient (mm^{-1})	19.810
F(000)	10336
Theta range for data collection	2.28 to 19.80°
Index ranges	$-17 \leq h \leq 17, -17 \leq k \leq 17, -22 \leq l \leq 22$
Reflections collected	24940
Independent reflections	7581 [R(int) = 0.2025]
Data/restraints/parameters	7581/0/230
Goodness-of-fit on F^2	1.281
Final R indices; 3202 data; I>2σ(I)	R1 = 0.1590, wR2 = 0.3994
Absolute structure parameter	0.55(18)
Largest diff. peak and hole	5.997 and -4.147 eÅ^{-3}

Table S1. Crystal data and structure refinement details for InSeI (this work).

Atom	Wyck.	x/a	y/b	z/c	U [Å^2]
I1	4h	0.6507(10)	0.4705(9)	0.0177(8)	0.042(5)
I2	4h	0.5338(13)	0.3708(13)	0.1790(12)	0.081(8)
I3	4h	0.6406(8)	0.0308(8)	0.0709(7)	0.027(4)
I4	4h	0.9737(10)	0.3434(10)	0.1258(9)	0.045(6)
I5	4h	0.8344(10)	0.0278(10)	0.2291(9)	0.047(6)
I6	4h	0.5247(9)	0.1786(10)	0.3306(8)	0.050(6)
I7	4h	0.8759(11)	0.4623(10)	0.2863(9)	0.059(6)
I8	4h	0.9446(14)	0.0951(14)	0.3960(12)	0.111(9)
I9	4h	0.9776(14)	0.2391(15)	0.5382(13)	0.116(9)
I10	4h	0.5280(12)	0.3338(12)	0.7537(10)	0.071(7)
I11	4h	0.7076(12)	0.4785(12)	0.4334(11)	0.088(7)
I12	4h	0.5594(15)	0.0836(15)	0.5049(13)	0.12(1)
I13	4h	0.6069(12)	0.4610(12)	0.6101(11)	0.082(7)
I14	4h	0.967(1)	0.3786(10)	0.7084(9)	0.054(6)
I15	4h	0.8645(11)	0.034(1)	0.8082(9)	0.055(6)
I16	4h	0.9727(11)	0.1476(11)	0.9655(10)	0.056(6)
I17	4h	0.845(1)	0.4733(10)	0.8598(9)	0.045(5)
I18	4h	0.5298(9)	0.1411(9)	0.9158(8)	0.043(5)
I19	4h	0.6920(12)	0.0253(12)	0.6461(10)	0.079(7)
In1	4h	0.7174(9)	0.3586(9)	0.0582(8)	0.026(5)
In2	4h	0.6532(9)	0.3053(9)	0.2109(8)	0.028(5)
In3	4h	0.6936(9)	0.1488(9)	0.1086(8)	0.023(5)
In4	4h	0.8581(8)	0.2745(8)	0.1592(7)	0.015(4)
In5	4h	0.7687(10)	0.140(1)	0.2693(9)	0.037(6)
In6	4h	0.6419(8)	0.2384(8)	0.3689(7)	0.016(4)
In7	4h	0.8187(9)	0.3420(9)	0.3200(8)	0.028(5)
In8	4h	0.8352(11)	0.1750(11)	0.4281(10)	0.054(6)

In9	4h	0.8522(8)	0.2396(8)	0.5818(7)	0.019(4)
In10	4h	0.7511(10)	0.3585(10)	0.4800(9)	0.037(5)
In11	4h	0.6539(8)	0.1797(8)	0.5324(7)	0.025(5)
In12	4h	0.6928(10)	0.3571(10)	0.6399(9)	0.041(6)
In13	4h	0.8566(9)	0.3038(9)	0.7425(8)	0.023(5)
In14	4h	0.7921(9)	0.1419(10)	0.8483(8)	0.029(5)
In15	4h	0.8503(9)	0.2044(8)	1.0015(8)	0.021(5)
In16	4h	0.8001(8)	0.3508(8)	0.9004(7)	0.016(4)
In17	4h	0.6441(9)	0.2137(9)	0.9501(7)	0.022(5)
In18	4h	0.7182(10)	0.1505(10)	0.6916(9)	0.043(6)
In19	4h	0.6487(9)	0.2829(9)	0.7917(8)	0.025(5)
Se1	4h	0.7545(10)	0.3672(10)	0.1615(8)	0.001(5)
Se2	4h	0.6544(14)	0.1709(15)	0.2072(13)	0.038(8)
Se3	4h	0.8342(12)	0.1600(12)	0.1067(11)	0.020(6)
Se4	4h	0.8741(15)	0.2296(14)	0.2600(13)	0.043(8)
Se5	4h	0.7278(12)	0.1319(12)	0.3698(10)	0.018(6)
Se6	4h	0.6795(11)	0.3480(11)	0.3148(10)	0.015(6)
Se7	4h	0.8561(14)	0.3027(13)	0.4184(12)	0.037(8)
Se8	4h	0.7887(14)	0.1411(14)	0.5280(12)	0.040(8)
Se9	4h	0.7988(12)	0.3636(12)	0.5774(11)	0.026(7)
Se10	4h	0.6314(15)	0.2937(14)	0.4703(13)	0.042(8)
Se11	4h	0.6323(14)	0.2322(13)	0.6313(11)	0.031(7)
Se12	4h	0.7371(12)	0.3655(12)	0.7422(10)	0.018(6)
Se13	4h	0.8734(12)	0.2562(12)	0.8416(10)	0.018(6)
Se14	4h	0.7544(12)	0.1340(12)	0.9516(10)	0.019(6)
Se15	4h	0.8394(13)	0.3353(13)	0.9994(12)	0.031(7)
Se16	4h	0.6583(12)	0.3317(12)	0.8966(11)	0.017(6)
Se17	4h	0.6275(15)	0.2546(15)	0.0504(12)	0.043(8)

|					
Se18	4h	0.8541(12)	0.1820(12)	0.6823(11)	0.027(7)
Se19	4h	0.6746(16)	0.1582(16)	0.7906(14)	0.048(8)

Table S2. Atomic coordinates and isotropic (U_{eq}) displacement parameters for InSeI as obtained in this work from InSeI single crystal analysis.
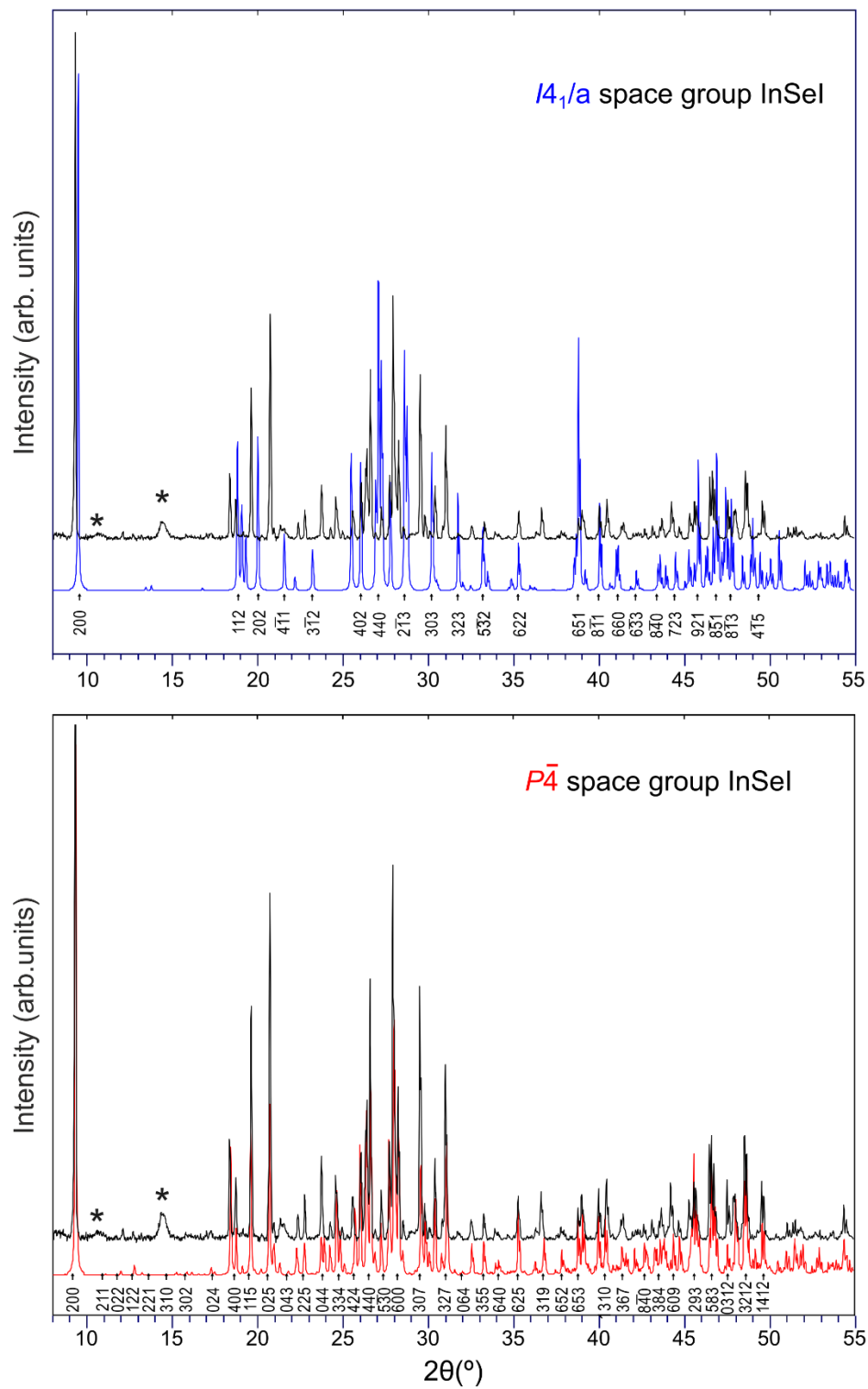
Fig. S2. Experimental X-ray powder diffraction pattern of InSeI (black spectra) compared to the theoretical pattern for the $I4_1/a$ polymorph from literature data[1] (CCDC 1659815) (top, blue

spectrum) and for the $P\bar{4}$ polymorph, the model of which was obtained in this work (bottom, red spectrum). The broad peaks labelled with * are due to Kapton foils used for the measurement.

Atomic force microscopy: AFM topography images of InSeI NWs on SiO₂/Si substrates were acquired in non-contact tapping mode with a Bruker JPK NanoWizard®V using Nanosensors[TM] NCHR Al-coated, highly-doped Si tips with resonance frequency 330 kHz and force constant 42 N/m.
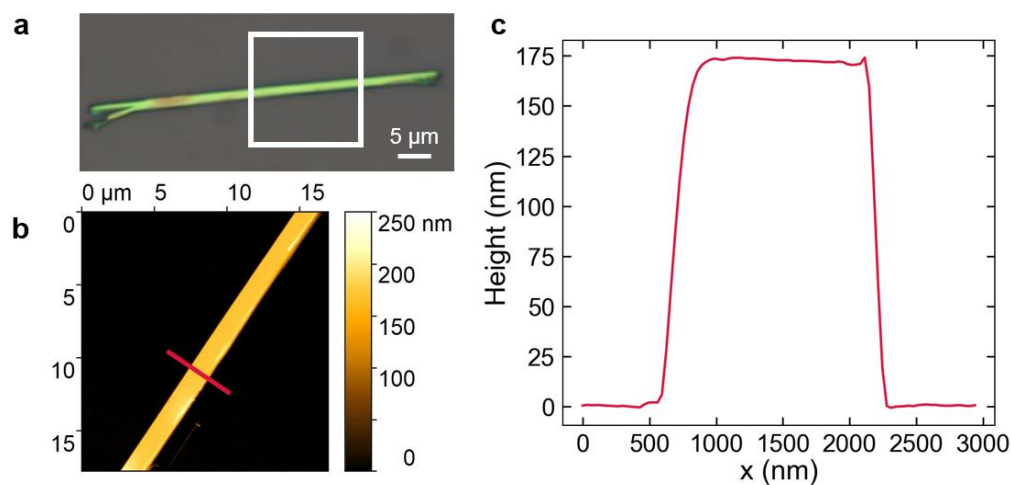

Fig. S3: Representative atomic force microscopy (AFM) characterization used to determine the range of thickness of the NWs under study. a) Optical microscope image of the NW. b) AFM scan of the region highlighted in panel a. c) Line profile of the indicated region on panel b, showing the height of the NW to be around 175 nm. Studied NWs show a thickness ranging from 40 to 500 nm.
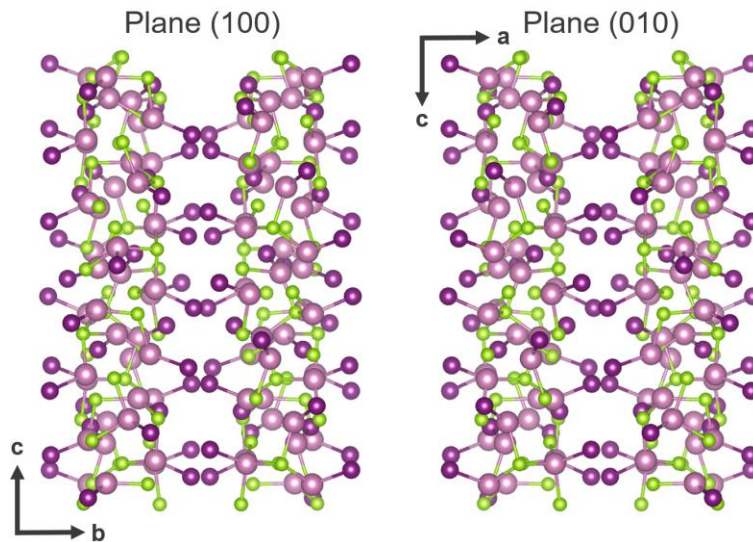
Fig. S4: Visualization of the (100) and (010) planes, showing mirror imaging along the *c*-axis, which makes these planes indistinguishable, i.e., equivalent.
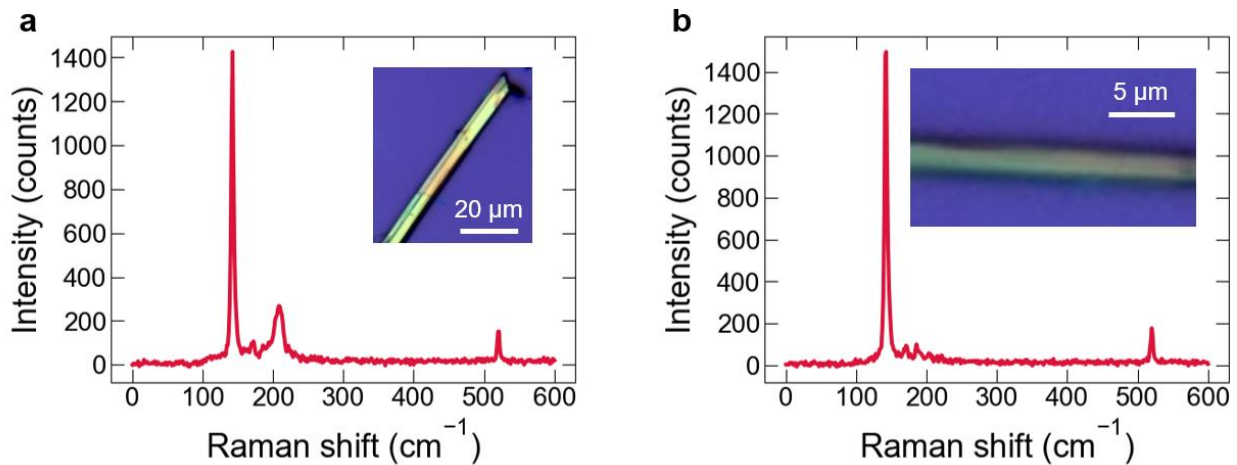

Fig. S5: Comparison between the Raman spectra of a) a thicker and b) a thinner NW, showing a decrease in intensity of the modes over 143 cm^{-1} as the NW thins down. Eventually, for thinner samples only mode 1 centered at 143 cm^{-1} is visible. The Raman mode observed at 520.5 cm^{-1} corresponds to the SiO$_2$/Si substrate.

Control experiments

Before carrying out the complete Raman spectroscopy characterization of the bulk InSeI crystals, we confirmed that by lowering the temperature the Raman modes just systematically

shift towards higher frequencies and sharpen (Fig. S6). This is relevant for comparing Raman measurements carried out at room temperature and 80 K.
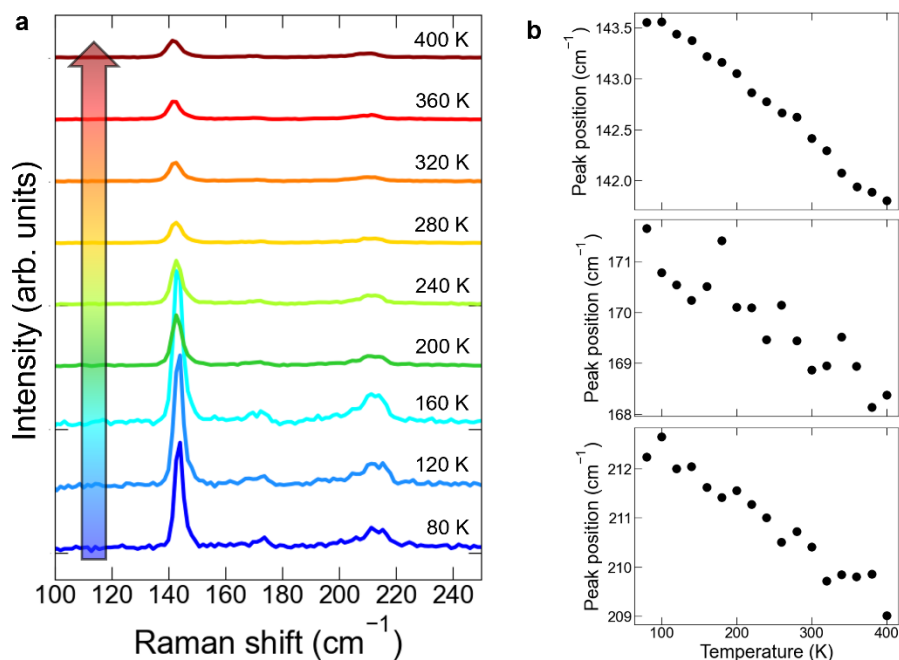
Fig. S6: (a) Representative Raman spectra collected in a bulk InSeI crystal at selected temperatures in the range (80 K-400 K) showing the characteristic modes. (b) Temperature evolution of the peak position of three selected modes showing a systematic shift towards higher frequencies when cooling down.

To corroborate the linearly polarized set-up implemented in the micro-Raman instrument keeping the polarization fixed and rotating the sample, we carried out tests using as a reference Si (100) and collecting the corresponding signal. In Fig. S7, we display the corresponding polar plots obtained in the VV and HV configurations showing the expected four loops and a 45º shift between them.

$$I_{VV} = I_0 \cdot \cos^2(2\theta)$$

$$I_{HV} = I_0 \cdot \sin^2(2\theta)$$
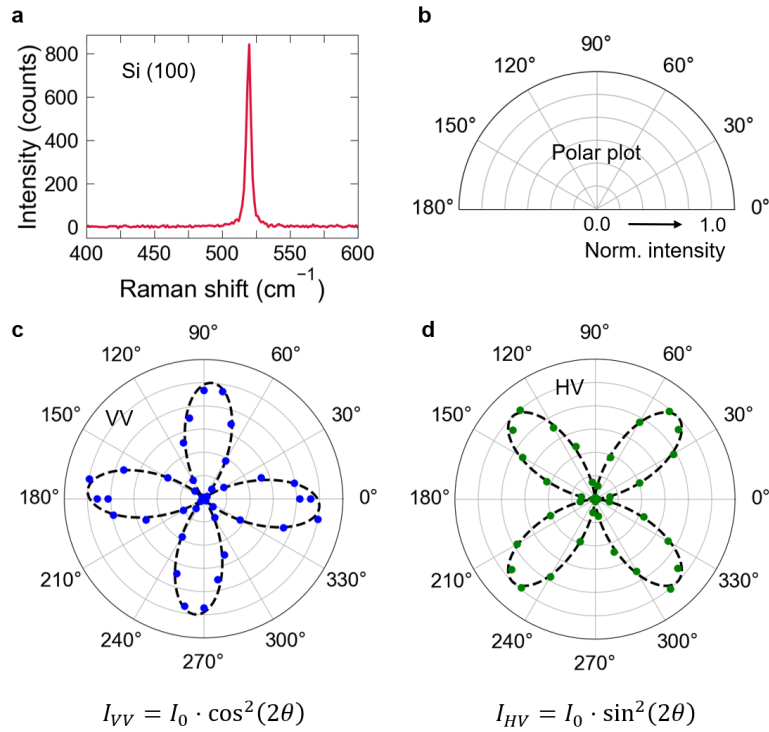
Fig. S7: a) Representative Raman spectrum of Si (100). b) Half normalized polar grid indicating the values of the radial-axis. c-d) Normalized polar plots from the integrated intensity of the characteristic 520.5 cm^{-1} peak rotating the Si/SiO$_2$ substrate and collecting the signal using the parallel (VV) and cross (HV) configurations, with the corresponding analysis as dashed lines.

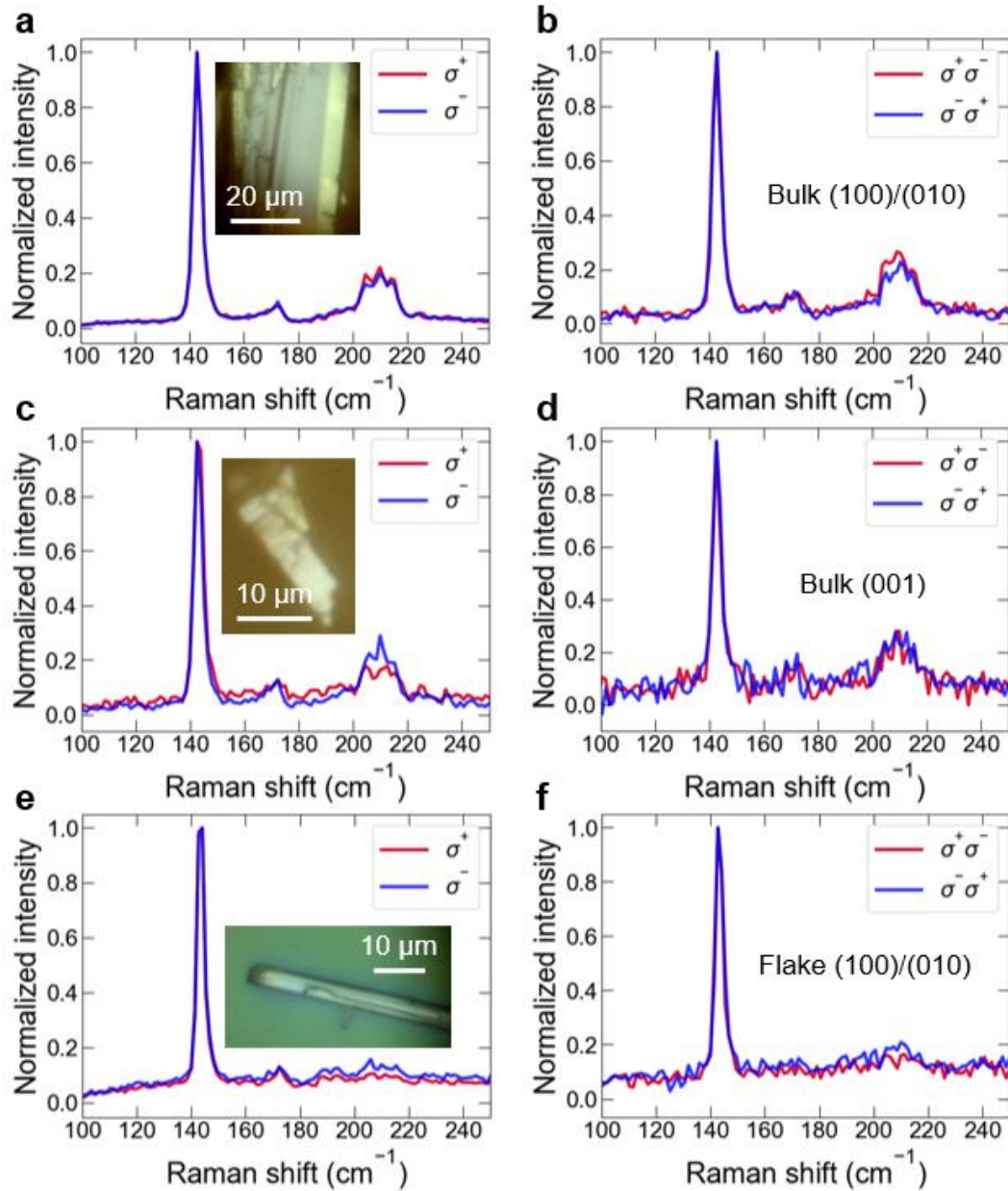**Additional polarized Raman spectroscopy analysis**

It is important to note that the polar plots shown in main text and SI are normalized to the maximum value. Therefore, it is possible to observe a finite intensity in the plots even for the modes expected to be zero from theory. The absolute intensity in these cases is at least one order of magnitude smaller than the intensity of the modes that are expected to be different from zero.
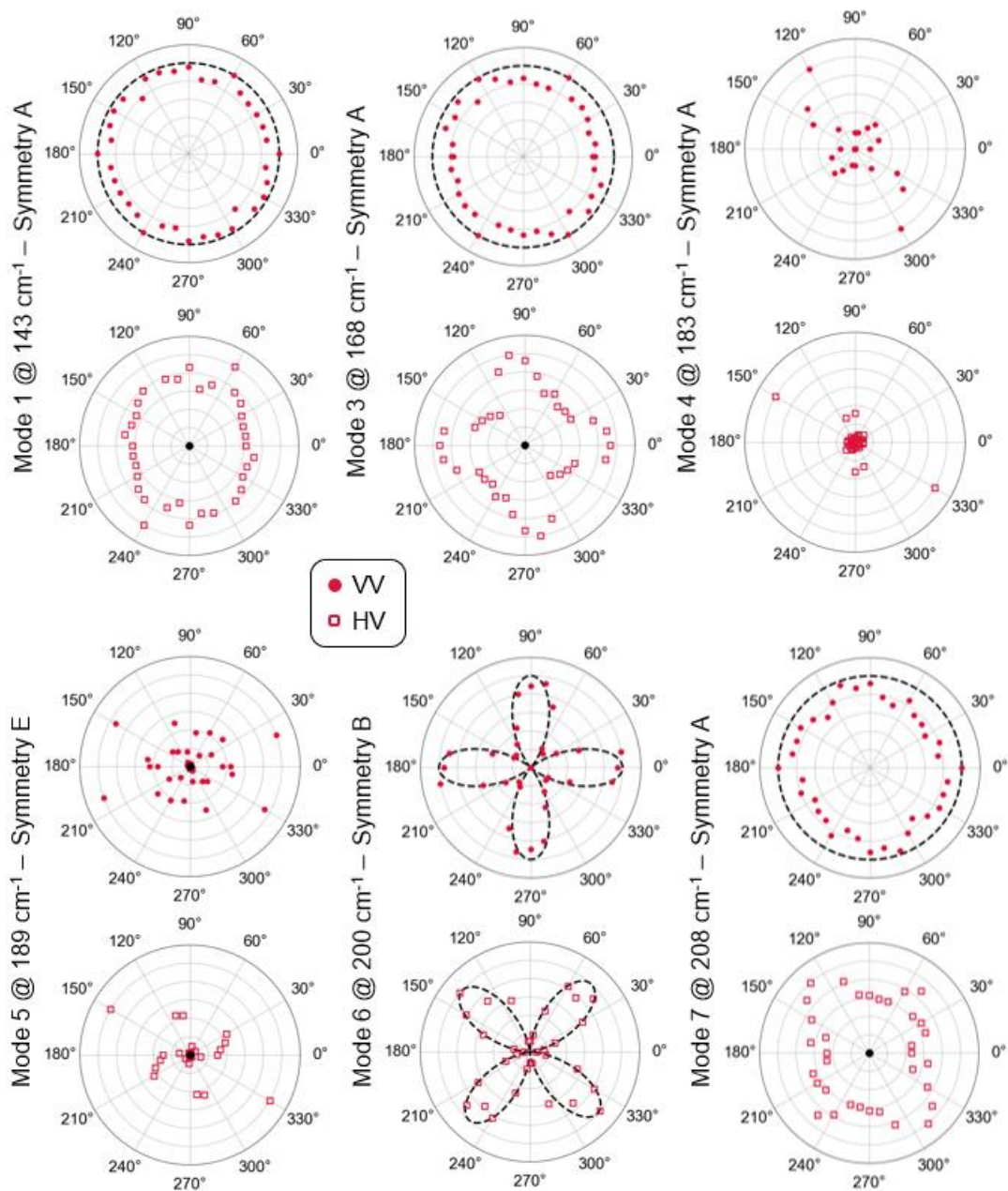
Fig. S8: Normalized polar plots showing the angle-dependence of the intensity of each Raman mode, under the VV and HV configurations, for the (001) plane. Experimental data are shown in full dots for the VV configuration and in empty squares for the HV configuration, while calculated data is shown as a black dashed line. The symmetry of the modes is assigned by comparison to the calculations (see Raman tensor analysis section below).
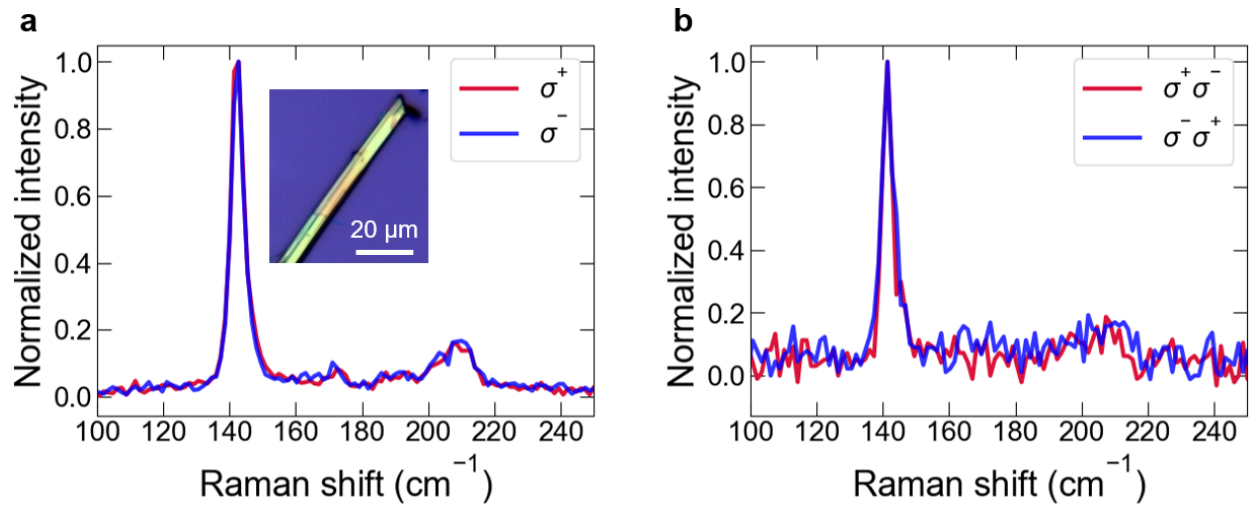
Fig. S9: Room temperature circularly polarized and helicity-resolved Raman spectroscopy characterization of NWs. a-b) Comparison between the normalized Raman spectra (to the 143 cm^{-1} mode) taken under the configurations σ^+ vs σ^-, and $\sigma^+\sigma^-$ vs $\sigma^-\sigma^+$, for incidence in the (100)/(010) planes.

Fig. S10: Circularly polarized and helicity-resolved Raman spectroscopy characterization at 80 K of a-d) bulk crystals and e-f) NWs. a-b) Comparison between the normalized Raman spectra (to the 143 cm^{-1} mode) taken under the configurations σ^+ vs σ^-, and $\sigma^+\sigma^-$ vs $\sigma^-\sigma^+$, for incidence along the (100)/(010) planes in a bulk crystal. c-d) Comparison between the normalized Raman spectra (to the 143 cm^{-1} mode) taken under the configurations σ^+ vs σ^-, and $\sigma^+\sigma^-$ vs $\sigma^-\sigma^+$, for incidence in the (001) plane in a bulk crystal. e-f) Comparison between the normalized Raman

spectra (to the 143 cm^{-1} mode) taken under the configurations σ^+vs σ^-, and $\sigma^+\sigma^-$ vs $\sigma^-\sigma^+$, for incidence in the (100)/(010) plane in a NW.

Raman tensor analysis: linearly polarized Raman and crystallographic planes

To calculate the pattern of azimuth rotation in backscattering configuration we start from the Raman tensors of the point group S_4,[2] corresponding to the space group identified by XRD. Note that the same tensor occurs for the case of the point group C_{4h},[2] also reported for this material. Thus, this analysis is valid for InSeI tetragonal crystal structures with space groups $I4_1/a$ (no. 88)[1,3] and the one reported here $P\overline{4}$ (no. 81). The differences are the notation of the representations: S_4 (A, B, E) and C_{4h} (A$_g$, B$_g$, E$_g$); and the number of active modes expected. In accordance with group theory, for InSeI crystal's symmetry (point group S_4, Wyckoff position *4h* (x, y, z)), there are 684 Raman active modes derived from 57 occupied *4h* Wyckoff positions, with irreducible representation $\Gamma = (3 \cdot 57)$ A + $(3 \cdot 57)$ B + $(3 \cdot 57)$ ^{1}E + $(3 \cdot 57)$ ^{2}E. While, for the InSeI (point group C_{4h}, Wyckoff position *16f*), there are 72 Raman active modes from 6 occupied *16f* Wyckoff positions, with irreducible representation $\Gamma = (3 \cdot 6)$ A$_g$ + $(3 \cdot 6)$ B$_g$ + $(3 \cdot 6)$ ^{1}E$_g$ + $(3 \cdot 6)$ ^{2}E$_g$.[4–7] Then the tensors are rotated to align the crystal orientation, and the patterns reported as polar plots are obtained for parallel (VV) and perpendicular (HV) polarization.[8–10] The tensors in their standard orientation[6,7] are reported below:

$$R\left(A \text{ or } A_g\right) = \begin{pmatrix} a & & \\ & a & \\ & & b \end{pmatrix}, R\left(B \text{ or } B_g\right) = \begin{pmatrix} c & d & \\ d & -c & \\ & & \end{pmatrix},$$

$$R\left(^1E \text{ or } ^1E_g\right) = \begin{pmatrix} & & e \\ & & f \\ e & f & \end{pmatrix}, R\left(^2E \text{ or } ^2E_g\right) = \begin{pmatrix} & & -f \\ & & e \\ -f & e & \end{pmatrix}$$

Finally, the angular dependent intensity is normalized over the angular range $(0,\pi)$ to simplify the analysis of the data eliminating an overall intensity constant.[9]
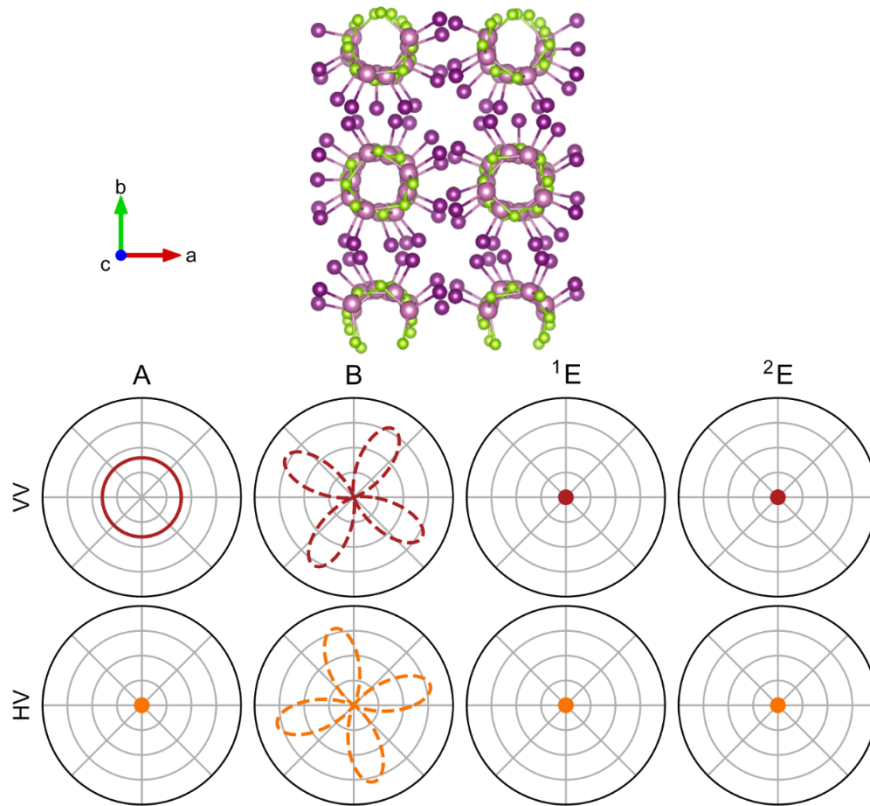
When the laser is incident in the (001) plane, the normalized intensity for the different representations is given by:

$$I_A^{VV}(\theta) = 1/\pi, I_A^{HV}(\theta) = 0$$

$$I_B^{VV}(\theta) = (2/\pi)\cos^2(2\theta - \phi), I_B^{HV}(\theta) = (2/\pi)\sin^2(2\theta - \phi), \phi = \arctan(d/c)$$

$$I_E^{VV}(\theta) = I_E^{HV}(\theta) = 0$$

where VV and HV are the configuration of polarizer and analyzer as discussed in the main text.

Fig. S11: Polarized Raman spectroscopy with incidence in the (001) plane. The upper panel shows the crystal structure in this alignment. The bottom panels are polar plots of normalized intensity as a function of the azimuth angle, for different representations of the S_4 point group. The horizontal direction corresponds to the *a* axis [100], as in the upper panel. The alignment with respect to the axes of the quadrupolar pattern of representation B depends on the parameters *c,d* of the Raman tensor; for this reason, it is shown as dashed lines (here with *c=1, d=-1.8).*

Only A and B modes are active while E are not. The A modes are constant in VV configuration and are zero in HV. In the B case, both VV and HV have a quadrupolar pattern with 45º shift, and their orientation with respect to the axes depends on the value of the parameters c and d.

In the tetragonal symmetry of the crystal, incidence in the (100) or (010) plane gives the same pattern, calculated as before:

$$I_{Ag}^{VV}(\theta) = \frac{8(a\sin^2(\theta) + b\cos^2(\theta))^2}{\pi(3a^2 + 2ab + 3b^2)}, I_{Ag}^{HV}(\theta) = \frac{2\sin^2(2\theta)}{\pi}$$

$$I_{Bg}^{VV}(\theta) = \frac{8\sin^4(\theta)}{3\pi}, I_{Bg}^{HV}(\theta) = \frac{2\sin^2(2\theta)}{\pi}$$

$$I_{Eg}^{VV}(\theta) = \frac{2\sin^2(2\theta)}{\pi}, I_{Eg}^{HV}(\theta) = \frac{2\cos^2(2\theta)}{\pi}$$
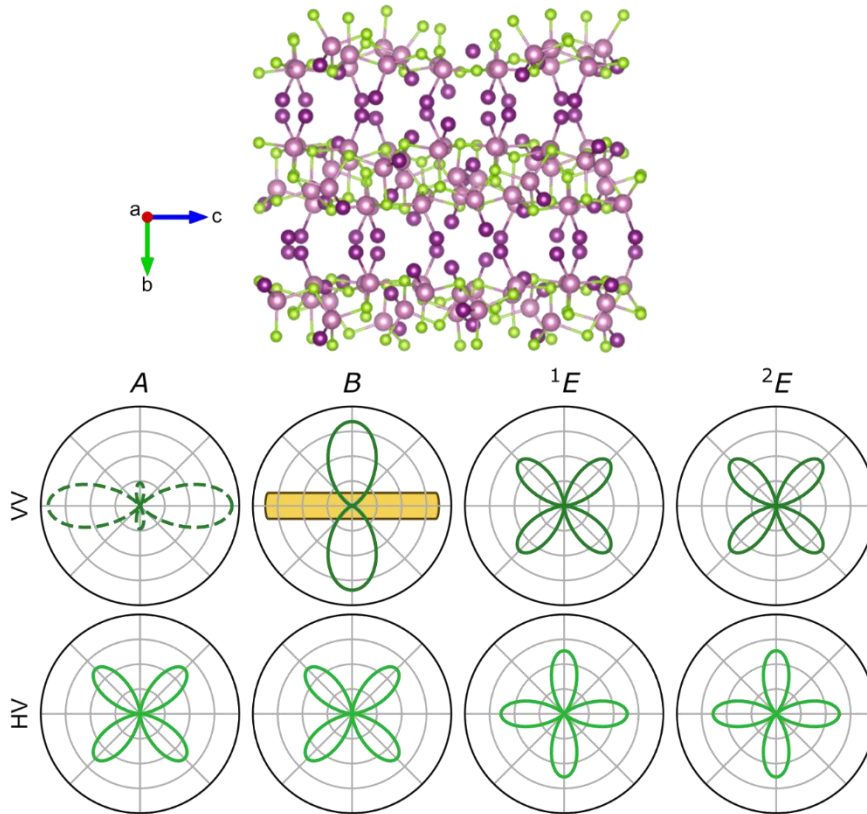
Fig. S12: Polarized Raman spectroscopy with incidence in the (100) plane. The upper panel shows the crystal structure in this alignment. The bottom panels are polar plots of normalized intensity

as a function of the azimuth angle, for different representations of the S_4 point group. The horizontal direction corresponds to the corresponds to the *c* axis [001], as in the upper panel. The yellow rectangle marks the alignment of the flake as in Fig. 3 of the main text. For the A representation in VV configuration (shown as a dashed line), the pattern depends on the parameters *a,b* of the Raman tensor (here with *a=1, b=-2).*

In this orientation, as shown in the Fig. S12, the pattern of A modes in VV configuration depends on the value of the parameters *a* and *b*, and can assume a variety of shape from quadrupolar to dipolar; in HV configuration, the pattern is always quadrupolar and has zeroes in the [001] and [010] directions. The other cases are independent of the parameters. The B case is dipolar in VV, with zeroes aligned with the [001] direction, and has the same quadrupolar pattern of A in HV. Both E modes have the same patterns: in VV they have zeroes along the [001] and [010] directions, in HV the zeroes are shifted by 45º.

References:

1 G. Sawitzki, D. Müller and H. Hahn, *Mater. Res. Bull.*, 1980, **15**, 753–762.
2 M. I. Aroyo, Ed., *International Tables for Crystallography: Space-group symmetry*, International Union of Crystallography, Chester, England, 2nd edn., 2016, vol. A.
3 R. Kniep and W. Welzel, *Z. Für Naturforschung B*, 1985, **40**, 26–31.
4 A. S. Pine and G. Dresselhaus, *Phys. Rev. B*, 1971, **4**, 356–371.
5 M. I. Aroyo, J. M. Perez-Mato, C. Capillas, E. Kroumova, S. Ivantchev, G. Madariaga, A. Kirov and H. Wondratschek, *Z. Für Krist. - Cryst. Mater.*, DOI:10.1524/zkri.2006.221.1.15.
6 M. I. Aroyo, A. Kirov, C. Capillas, J. M. Perez-Mato and H. Wondratschek, *Acta Crystallogr. A*, 2006, **62**, 115–128.
7 M. I. Aroyo, J. M. Perez-Mato, D. Orobengoa, E. Tasci, G. de la Flor and A. Kirov, *Bulg. Chem. Commun.*, 2011, **43**, 183–197.
8 D. Spirito, S. Marras and B. Martín-García, *J. Mater. Chem. C*, 2024, **12**, 2544–2551.
9 B. Martín-García, D. Spirito, M. Lin, Y. Leng, S. Artyukhin, P. Tan and R. Krahne, *Adv. Opt. Mater.*, 2022, **10**, 2200240.
10 X.-L. Liu, X. Zhang, M.-L. Lin and P.-H. Tan, *Chin. Phys. B*, 2017, **26**, 067802.